RSC Advances

PAPER

View Article Online
View Journal | View Issue

Cite this: *RSC Adv.*, 2026, **16**, 8453

Fluorescent-state switching of a 10-hydroxybezo[*h*]quinoline skeleton through the electronic nature of substituents

Marino Miwa[a] and Akitaka Ito *[ab]

Received 1st December 2025
Accepted 28th January 2026

DOI: 10.1039/d5ra09266c

rsc.li/rsc-advances

The spectroscopic and photophysical properties of novel 10-hydroxybenzo[*h*]quinoline (HBq) derivatives with various *para*-substituted phenyl groups at the 7- and 9-positions (1R; R = $-NMe_2$, $-OMe$, $-Me$, $-H$, $-F$, $-Cl$, $-CF_3$, $-CN$, and $-NO_2$) were evaluated by the electron-donating and electron-withdrawing ability of the substituent R in terms of the Hammett substituent constant. The electronic nature of the substituents controlled the excited-state properties. In particular, **1NO$_2$** exhibited a larger nonfluorescence rate constant than that predicted from the energy gap dependence, and the fluorescence from **1NO$_2$** was solvent-dependent, distinct from that of the other derivatives. The TD-DFT calculations revealed that the excited-state derivatives except for **1NO$_2$** adopted the keto-form structures generated by ESIPT, whereas **1NO$_2$** exhibited non-ESIPT excited-state geometry. The difference originates from the variation in the charge-transfer characters: in the former, charge transfer occurs within the HBq moiety, whereas in the latter, charge transfer proceeds from the HBq moiety to the 4-nitrophenyl groups. The systematic tuning of the electronic transition demonstrated control of the excited-state geometry of HBq derivatives and provided important insights into proton transfer in the excited state. The introduction of 4-substituted phenyl groups also controlled the basicity of the derivatives in the ground states and, notably, **1NMe$_2$** exhibited pronounced fluorescence color variations, ranging from the near-infrared to the blue region, as a function of the concentration of trifluoroacetic acid.

Introduction

Owing to their applicability in photochemical applications, such as fluorescent probes, organic light-emitting diodes and fluorescent sensors, a variety of organic fluorophores have been developed based on their chemical and electronic structures.[1–4] The structure of a molecule in the light-emitting state is different from that in the ground state. For example, the C–C bond lengths of aromatic hydrocarbons (*i.e.*, benzene and anthracene) are elongated in the excited state upon the electronic transition from the bonding π-orbital to the antibonding π*-orbital. As an intriguing example, 4-(*N*,*N*-dimethylamino) benzonitrile is known to exhibit dual fluorescence arising from two structurally distinct excited states: locally-excited (LE) state, with a planar structure similar to the ground state, and twisted intramolecular charge transfer (TICT) state, in which the dimethylamino group is twisted.[5] These TICT-type dual fluorescent systems were utilized as chemical probes to achieve sensitive and quantitative detection on the basis of the TICT/LE fluorescence intensity ratio.[6] In addition to the TICT systems, dynamic structural changes in the excited state have been exploited for multicolor fluorescence from single chemical species,[7,8] fluorescent probes for the surrounding environment[9] and related applications. Thus, controlling the excited-state structure is one of the most important factors in fine tuning the emission characteristics of fluorophores and their applications.

Excited-state intramolecular proton transfer (ESIPT) is an excited-state isomerization process in which a hydrogen atom or an ion migrates to a different position in a molecule. It was reported by Weller in the 1950s that salicylic acid has a large absorption–fluorescence energy difference ($\Delta\tilde{\nu}$) compared to that of methyl salicylate and was attributed to the proton migration between the hydroxy and carboxy groups upon electronic transition owing to the difference in their acidities.[10,11] Since the isomerization process strongly stabilizes the excited state energetically, resulting in a large $\Delta\tilde{\nu}$, ESIPT-type compounds can emit efficiently even in the aggregated state by avoiding self-absorption. In practice, 2-(2-hydroxyphenyl) benzothiazole (HBT), a representative ESIPT-type compound, exhibits intense green fluorescence in the solid state (fluorescence quantum yield $\Phi_f = 0.38$)[12] with a large $\Delta\tilde{\nu}$ of ~9300 cm^{-1}.[13] Therefore, ESIPT-type compounds have recently attracted increasing attention as a strategy to enhance the $\Delta\tilde{\nu}$

[a]*Graduate School of Engineering, Kochi University of Technology, Miyanokuchi 185, Tosayamada, Kami, Kochi 782-8502, Japan. E-mail: ito.akitaka@kochi-tech.ac.jp*
[b]*Research Center for Advanced Chiral Optical Materials (RACOMs), Research Institute, Kochi University of Technology, Miyanokuchi 185, Tosayamada, Kami, Kochi 782-8502, Japan*

toward solid-state fluorophores. As examples, compounds exhibiting significant zwitterionic character were reported by Yamaguchi and coworkers.[14,15] Furthermore, unique ESIPT-based molecules have been developed, including those exhibiting near-infrared emission[16–18] and involving multiple proton transfer processes.[19,20] In contrast to such fascinating properties, reports on ESIPT-type compounds are limited to a few structural classes, such as HBTs,[21–23] benzophenones,[24] anthraquinones[25–28] and flavones.[29] This fact highlights the importance of achieving a unified understanding of the chemical/electronic structures dominating ESIPT and elucidating the proton-transfer mechanism. Systematic modulation of the electronic structures of an ESIPT-type skeleton has not, however, been performed since most ESIPT-type compounds are less or non-emissive in diluted solutions (*e.g.*, $\Phi_f = 0.005$ for HBT in benzene).[23]

We focused on 10-hydroxybenzo[*h*]quinoline (HBq), an ESIPT-type molecule,[30] as a target skeleton in the present study. As shown in Fig. S1, both absorption and fluorescence spectra of HBq are completely different from those of benzo[*h*]quinoline without a hydroxy group. HBq exhibits fluorescence with a large $\Delta\tilde{\nu}$ of 11 300 cm^{-1}, and the Φ_f value in diluted solution (0.018 in THF) is satisfactorily large to detect owing to its structural rigidity. These properties allow us to perform photophysical studies in a diluted solution. Prior to the experiment, theoretical calculations using density functional theory (DFT) and time-dependent DFT (TD-DFT) were performed for HBq as shown in Fig. S3. Structural optimizations and Gibbs-energy evaluations at fixed O–H distances revealed that the enol form with an O–H bond is the most stable in the electronic ground state and that the keto form with an N–H bond is the most stable in the lowest-energy singlet excited (S_1) state. The results strongly suggest the existence of the ESIPT process. The S_1 absorption transition that triggers ESIPT was ascribed to a HOMO → LUMO transition. The HOMO of HBq corresponds to the π-orbital with a large contribution of the oxygen atom, while the LUMO populates the nitrogen atom more. As a result, the S_1 state of HBq is ππ* with a weak charge-transfer character, and the electron densities of the oxygen and nitrogen atoms decrease and increase, respectively, upon photoexcitation. Therefore, it can be expected that the ESIPT process corresponds to an intramolecular acid–base reaction between the photoacidic hydroxy and photobasic imine moieties and that the proton-transfer process is controllable by tuning the charge-transfer character within the HBq moiety. In this study, we designed and synthesized novel HBq derivatives with various *para*-substituted phenyl (4-Rphenyl) groups at the 7- and 9-positions of HBq (1R; R = –NMe_2, –OMe, –Me, –H, –F, –Cl, –CF_3, –CN, –NO_2, see Scheme 1). Since the substituents R were introduced *via* the phenylene moiety to avoid steric repulsion between the benzo[*h*]quinoline backbone and substituents, the spectroscopic and photophysical properties of 1R could be evaluated by the electron-donating and -withdrawing ability of the substituent R in terms of the Hammett substituent constant (σ_p).[31] Through the systematic variation of σ_p, the charge-transfer character to give the S_1 state of a derivative was successfully tuned, and **1NO$_2$** with strong electron-withdrawing nitro groups exhibited non-ESIPT fluorescence.

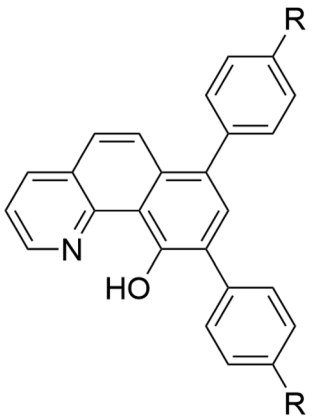

Scheme 1 Chemical structures of 1R (R = –NMe_2, –OMe, –Me, –H, –F, –Cl, –CF_3, –CN, and –NO_2).

Experimental

Synthesis and characterization

Reagents purchased from FUJIFILM Wako Pure Chemical Corporation, Tokyo Chemical Industry Co., Ltd or NACALAI TESQUE, Inc. were used for synthesis as supplied. Reaction products were purified by column chromatography by using silica gel 60 (particle size: 63–210 μm, KANTO CHEMICAL Co., Inc.), medium-pressure column chromatography (stationary phase: Yamazen Science Inc., universal column premium silica gel 30 μm and inject column silica gel, flow rate: 40 mL min^{-1}) or gel-permeation chromatography (Japan Analytical Industry preparative recycling chromatography LC908 System, stationary phase: JAIGEL-1H × 2 + JAIGEL-2H × 1, flow rate: 3.5 mL min^{-1}, eluent: HPLC-grade chloroform with 0.3 vol% triethylamine). Thin-layer chromatography was performed using silica gel 60 F_{254}, neutral, on aluminum sheets (Merck Millipore), and spots were visualized using an ASONE SLUV-6 handy UV lamp. Melting points of the compounds were determined using an MPA100 melting point apparatus (Stanford Research Systems). ^{1}H-NMR spectra in $CDCl_3$ (NMR grade, KANTO CHEMICAL Co., Inc.) were recorded on a JEOL JMN-ECZ400S spectrometer (399.78 MHz). Chemical shifts of the spectra were reported in ppm with tetramethylsilane as an internal standard (0.00 ppm). Electrospray ionization mass spectrometry (ESI-MS) was performed by injecting a sample solution in acetonitrile containing 0.1 vol% formic acid into the mass detector of a Bruker compact QTOF system. Infrared (IR) diffuse reflectance spectra of the compounds diluted in potassium bromide (KBr) were recorded on a Jasco FT/IR-4600 Fourier-transform infrared spectrometer.

A crystal of 1R (R = –NMe_2, –OMe, –Me, –H, –F and –CF_3) was picked up under an optical microscope and, then, single-crystal XRD measurements were performed using a Rigaku XtaLAB Synergy-S/Mo system (Mo Kα, $\lambda = 0.71073$ Å). X-ray diffraction data were collected at 93 K by a HyPix-600HE photon counting detector and analyzed using Olex2 crystallographic software

package.[32] The structure was solved by direct methods (ShelXT[33]) and refined through full-matrix least-squares techniques on F^2 using ShelXL.[34] All non-hydrogen atoms were refined with anisotropic displacement parameters. Hydrogen atoms were placed at calculated positions and refined "riding" on their corresponding carbon, nitrogen or oxygen atoms.

Synthesis of 7,9-diiodo-10-hydroxybenzo[*h*]quinoline ($\mathbf{HBqI_2}$). Synthesis was performed with minor changes in the report procedure.[35] After adding an aqueous solution of sodium carbonate (0.12 M (= mol dm^{-3}), 100 mL) to a solution of HBq (2.08 g, 10.7 mmol) in THF (100 mL) in an eggplant flask, iodine (13.2 g, 52.0 mmol) was added in several portions. The mixture was refluxed for 2 days. After being allowed to cool to ambient temperature, an aqueous solution of sodium thiosulfate (1.0 M, 100 mL) was added. Resulting precipitates were collected by suction filtration and washed with water (50 mL × 2). Purification by column chromatography (dichloromethane), followed by recrystallizations from toluene twice, afforded $\mathbf{HBqI_2}$ as orange needles (3.57 g, 75%). $R_f = 0.35$ (ethyl acetate/*n*-hexane = 1/4 (v/v)); m.p. 249.4 °C (decomposition); ^{1}H-NMR ($CDCl_3$): δ = 16.7 (s, 1H, OH), 8.86 (dd, 1H, J = 1.6, 4.8 Hz, 2-Ar–H), 8.57 (s, 1H, 8-Ar–H), 8.34 (dd, 1H, J = 1.6, 8.0 Hz, 4-Ar–H), 8.09 (d, 1H, J = 9.2 Hz, 5- or 6-Ar–H), 7.77 (d, 1H, J = 9.2 Hz, 5- or 6-Ar–H), 7.66 ppm (dd, 1H, J = 4.4, 8.0 Hz, 3-Ar–H); HRMS (ESI): calcd for $[M + H]^+$: m/z = 447.8690; found: 447.8689; IR (KBr): $\tilde{\nu}$ = 3072 (Ar), 3051 (Ar), 2442 (OH), 1508 (Ar), 1452 (Ar), 1421 (Ar), 1407 (Ar), 1392 (Ar), 1209 (Ar), 1127 (Ar), 1027 (Ar), 827 (Ar), 810 (Ar), 699 (Ar), 628 (Ar), 570 (Ar), 522 cm^{-1} (Ar).

7,9-Bis[4-(*N*,*N*-dimethylamino)phenyl]-10-hydroxybenzo[*h*]quinoline ($\mathbf{1NMe_2}$). Synthesis was performed by Suzuki–Miyaura cross coupling, similar to the literature report.[36] To a solution of $\mathbf{HBqI_2}$ (0.24 g, 0.54 mmol) and 4-(*N*,*N*-dimethylamino)phenylboronic acid (0.20 g, 1.2 mmol) in toluene (9 mL) in a three-necked round-bottom flask, an aqueous solution of Na_2CO_3 (2.0 M, 4 mL) was added. The biphase mixture was deaerated by bubbling argon gas for 15 minutes at ambient temperature. Tetrakis(triphenylphosphine)palladium(0) ($[Pd(PPh_3)_4]$, 0.02 g, 0.02 mmol) was added, and then, the mixture was refluxed for 70 h. After being allowed to cool to ambient temperature, water (50 mL) was added, and products were extracted with dichloromethane (50 mL × 4). The combined organic phase was washed with brine (100 mL), dried over anhydrous $MgSO_4$ and evaporated under reduced pressure. Purification by column chromatography (dichloromethane/*n*-hexane = 4/1 (v/v)), followed by repeated recrystallizations from acetonitrile, afforded $\mathbf{1NMe_2}$ as orange blocks (0.05 g, 22%). R_f = 0.38 (dichloromethane/*n*-hexane = 4/1 (v/v)); m.p. 252.7–255.4 °C; ^{1}H-NMR ($CDCl_3$): δ = 15.9 (s, 1H, OH), 8.79 (dd, 1H, J = 1.4, 4.6 Hz, 2-Ar–H of HBq), 8.24 (dd, 1H, J = 1.8, 7.8 Hz, 4-Ar–H of HBq), 8.02 (d, 1H, J = 9.2 Hz, 5- or 6-Ar–H of HBq), 7.76 (td, 2H, J = 2.7, 9.5 Hz, Ar–H of ph), 7.74 (s, 1H, 8-Ar–H of HBq), 7.56 (dd, 1H, J = 4.2, 8.2 Hz, 3-Ar–H of HBq), 7.53 (d, 1H, J = 4.2, 8.2 Hz, 5- or 6-Ar–H of HBq), 7.41 (td, 2H, J = 2.6, 9.2 Hz, Ar–H of ph), 6.88 (td, 4H, J = 2.4, 9.2 Hz, Ar–H of ph), 3.04 (s, 6H, NCH_3), 3.00 ppm (s, 6H, NCH_3); HRMS (ESI): calcd for $[M + H]^+$: m/z = 434.2227; found: 434.2190; IR (KBr): $\tilde{\nu}$ = 3095 (Ar), 3042 (Ar), 2982 (Ar), 2880 (CH), 2847 (CH), 2795 (Ar), 2697 (OH), 1610 (Ar), 1524 (Ar), 1499 (Ar), 1468 (Ar), 1444 (Ar), 1422 (Ar), 1396 (Ar), 1352 (C–N), 1314 (Ar), 1199 (Ar), 1123 (Ar), 1062 (Ar), 946 (Ar), 824 (Ar), 812 (Ar), 700 (Ar), 624 (Ar), 539 cm^{-1} (Ar).

Synthesis of 7,9-bis(4-methoxyphenyl)-10-hydroxybenzo[*h*]quinoline (1OMe). The reaction was performed similar to the synthesis of $\mathbf{1NMe_2}$ using $\mathbf{HBqI_2}$ (0.23 g, 0.51 mmol), 4-methoxyphenylboronic acid (0.19 g, 1.3 mmol), toluene (9 mL), aqueous Na_2CO_3 solution (1.9 M, 4 mL) and $[Pd(PPh_3)_4]$ (0.02 g, 0.02 mmol). After refluxing for 70 h, followed by neutralization with hydrochloric acid (0.5 M, 30 mL), products were extracted with dichloromethane (50 mL × 3). The combined organic phase was washed with brine (100 mL), dried over anhydrous $MgSO_4$ and evaporated under reduced pressure. Purification by column chromatography (dichloromethane), followed by recrystallizations from ethanol twice, afforded **1OMe** as orange needles (0.11 g, 56%). R_f = 0.38 (dichloromethane); m.p. 184.3–185.0 °C; ^{1}H-NMR ($CDCl_3$): δ = 16.0 (s, 1H, OH), 8.80 (dd, 1H, J = 1.6, 4.8 Hz, 2-Ar–H of HBq), 8.26 (dd, 1H, J = 1.8, 8.2 Hz, 4-Ar–H of HBq), 7.94 (d, 1H, J = 9.2 Hz, 5- or 6-Ar–H of HBq), 7.79 (td, 2H, J = 2.6, 9.4 Hz, Ar–H of ph), 7.70 (s, 1H, 8-Ar–H of HBq), 7.58 (dd, 1H, J = 4.8, 8.0 Hz, 3-Ar–H of HBq), 7.57 (d, 1H, J = 9.2 Hz, 5- or 6-Ar–H of HBq), 7.44 (td, 2H, J = 2.6, 9.2 Hz, Ar–H of ph), 7.04 (qd, 4H, J = 2.8, 4.5 Hz, Ar–H of ph), 3.90 (s, 3H, OCH_3), 3.88 ppm (s, 3H, OCH_3); HRMS (ESI): calcd for $[M + H]^+$: m/z = 408.1594; found: 408.1573; IR (KBr): $\tilde{\nu}$ = 3009 (Ar), 2963 (Ar), 2833 (Ar), 2541 (OH), 1607 (Ar), 1515 (Ar), 1498 (Ar), 1463 (Ar), 1395 (Ar), 1322 (Ar), 1284 (Ar), 1265 (Ar), 1248 (C–O–C), 1181 (Ar), 1121 (Ar), 1033 (C–O–C), 888 (Ar), 833 (Ar), 573 (Ar), 550 (Ar), 524 (Ar), 513 cm^{-1} (Ar).

Synthesis of 7,9-bis(4-methylphenyl)-10-hydroxybenzo[*h*]quinoline (1Me). The reaction was performed similar to the synthesis of $\mathbf{1NMe_2}$ using $\mathbf{HBqI_2}$ (1.15 g, 2.6 mmol), 4-methylphenylboronic acid (0.87 g, 6.4 mmol), toluene (40 mL), ethanol (15 mL), aqueous Na_2CO_3 solution (2.0 M, 20 mL) and $[Pd(PPh_3)_4]$ (0.12 g, 0.11 mmol). After refluxing for 45 h, followed by neutralization with hydrochloric acid (0.1 M, 250 mL), the products were extracted with dichloromethane (250 mL × 3). The combined organic phase was washed with brine (500 mL), dried over anhydrous $MgSO_4$ and evaporated under reduced pressure. Purification by column chromatography (dichloromethane/*n*-hexane = 1/1 (v/v)), followed by recrystallizations from dichloromethane/ethanol twice, afforded **1Me** as orange needles (0.25 g, 28%). R_f = 0.48 (dichloromethane/*n*-hexane = 1/1 (v/v)); m.p. 171.3–172.1 °C; ^{1}H-NMR ($CDCl_3$): δ = 16.0 (s, 1H, OH), 8.81 (dd, 1H, J = 1.4, 4.6 Hz, 2-Ar–H of HBq), 8.27 (dd, 1H, J = 2.0, 8.4 Hz, 4-Ar–H of HBq), 7.96 (d, 1H, J = 9.2 Hz, 5- or 6-Ar–H of HBq), 7.73 (td, 2H, J = 2.0, 8.0 Hz, Ar–H of ph), 7.72 (s, 1H, 8-Ar–H of HBq), 7.59 (dd, 1H, J = 4.4, 8.4 Hz, 3-Ar–H of HBq), 7.58 (d, 1H, J = 9.2 Hz, 5- or 6-Ar–H of HBq), 7.42 (td, 2H, J = 2.0, 8.2 Hz, Ar–H of ph), 7.31 (dd, 4H, J = 4.6, 7.8 Hz, Ar–H of ph), 2.47 (s, 3H, CH_3), 2.43 ppm (s, 3H, CH_3); HRMS (ESI): calcd for $[M + H]^+$: m/z = 376.1696; found: 376.1679; IR (KBr): $\tilde{\nu}$ = 3022 (Ar), 2918 (CH), 2862 (CH), 2472 (OH), 1513 (Ar), 1480 (Ar), 1394 (Ar), 1327 (Ar), 1206 (Ar), 1122 (Ar), 917 (Ar), 902 (Ar), 827 (Ar), 773 (Ar), 743 (Ar), 734 (Ar), 705 (Ar), 628 (Ar), 565 cm^{-1} (Ar).

Synthesis of 7,9-diphenyl-10-hydroxybenzo[*h*]quinoline (1H). The reaction was performed similar to the synthesis of $\mathbf{1NMe_2}$

using **HBqI$_2$** (0.68 g, 1.5 mmol), phenylboronic acid (0.44 g, 3.6 mmol), toluene (24 mL), ethanol (9 mL), aqueous Na_2CO_3 solution (2.1 M, 12 mL) and [Pd(PPh$_3$)$_4$] (0.06 g, 0.05 mmol). After refluxing for 45 h, followed by neutralization with hydrochloric acid (0.1 M, 205 mL), products were extracted with dichloromethane (150 mL × 3). The combined organic phase was washed with brine (300 mL), dried over anhydrous $MgSO_4$ and evaporated under reduced pressure. Purification by column chromatography (dichloromethane/*n*-hexane = 1/1 (v/v)), followed by recrystallizations from ethyl acetate/*n*-hexane twice, afforded **1H** as yellow needles (0.33 g, 63%). R_f = 0.48 (dichloromethane/*n*-hexane = 1/1 (v/v)); m.p. 186.8–188.7 °C; ^{1}H-NMR ($CDCl_3$): δ = 16.1 (s, 1H, OH), 8.83 (dd, 1H, J = 1.4, 4.6 Hz, 2-Ar–H of HBq), 8.29 (dd, 1H, J = 1.5, 8.0 Hz, 4-Ar–H of HBq), 7.96 (d, 1H, J = 9.2 Hz, 5- or 6-Ar–H of HBq), 7.85 (td, 2H, J = 1.6, 7.8 Hz, Ar–H of ph), 7.74 (s, 1H, 8-Ar–H of HBq), 7.61 (dd, 1H, J = 4.2, 8.6 Hz, 3-Ar–H of HBq), 7.60 (s, 1H, J = 8.8 Hz, 5- or 6-Ar–H of HBq), 7.55–7.47 (m, 6H, Ar–H of ph), 7.43 (tt, 1H, J = 1.7, 6.5 Hz, Ar–H of ph), 7.37 ppm (tt, 1H, J = 1.0, 7.4 Hz, Ar–H of ph); HRMS (ESI): calcd for [M + H]$^+$: m/z = 348.1383; found: 348.1367; IR (KBr): $\tilde{\nu}$ = 3051 (Ar), 3027 (Ar), 2592 (OH), 1609 (Ar), 1577 (Ar), 1504 (Ar), 1470 (Ar), 1437 (Ar), 1399 (Ar), 1325 (Ar), 1308 (Ar), 898 (Ar), 890 (Ar), 834 (Ar), 781 (Ar), 758 (Ar), 740 (Ar), 726 (Ar), 700 cm^{-1} (Ar).

Synthesis of 7,9-bis(4-fluorophenyl)-10-hydroxybenzo[*h*]quinoline (1F). The reaction was performed similar to the synthesis of **1NMe$_2$** using **HBqI$_2$** (0.24 g, 0.54 mmol), 4-fluorophenylboronic acid (0.16 g, 1.1 mmol), toluene (9 mL), aqueous Na_2CO_3 solution (1.9 M, 4 mL) and [Pd(PPh$_3$)$_4$] (0.02 g, 0.02 mmol). After refluxing for 45 h, followed by neutralization with hydrochloric acid (0.5 M, 50 mL), the products were extracted with dichloromethane (50 mL × 3). The combined organic phase was washed with brine (100 mL), dried over anhydrous $MgSO_4$ and evaporated under reduced pressure. Purification by column chromatography (dichloromethane/*n*-hexane = 1/1 (v/v)), followed by recrystallization from *n*-hexane (2 times) and ethanol, afforded **1F** as yellow needles (0.13 g, 62%). R_f = 0.50 (dichloromethane/*n*-hexane = 1/1 (v/v)); m.p. 181.1–181.3 °C; ^{1}H-NMR ($CDCl_3$): δ = 16.1 (s, 1H, OH), 8.84 (dd, 1H, J = 1.8, 4.6 Hz, 2-Ar–H of HBq), 8.31 (dd, 1H, J = 1.6, 8.0 Hz, 4-Ar–H of HBq), 7.89 (d, 1H, J = 9.2 Hz, 5- or 6-Ar–H of HBq), 7.83–7.78 (m, 2H, Ar–H of ph), 7.66 (s, 1H, 8-Ar–H of HBq), 7.62 (dd, 1H, J = 4.4, 8.0 Hz, 3-Ar–H of HBq), 7.62 (d, 1H, J = 9.2 Hz, 5- or 6-Ar–H of HBq), 7.50–7.45 (m, 2H, Ar–H of ph), 7.23–7.15 ppm (m, 4H, Ar–H of ph); HRMS (ESI): calcd for [M + H]$^+$: m/z = 384.1194; found: 384.1182; IR (KBr): $\tilde{\nu}$ = 3460 (Ar), 3043 (Ar), 2581 (OH), 1604 (Ar), 1514 (Ar), 1499 (Ar), 1473 (Ar), 1323 (Ar), 1224 (H–F), 1158 (Ar), 828 (Ar), 562 (Ar), 527 cm^{-1} (Ar).

Synthesis of 7,9-bis(4-chlorophenyl)-10-hydroxybenzo[*h*]quinoline (1Cl). The reaction was performed similar to the synthesis of **1NMe$_2$** using **HBqI$_2$** (0.24 g, 0.54 mmol), 4-chlorophenylboronic acid (0.20 g, 1.3 mmol), toluene (8 mL), ethanol (3 mL), aqueous Na_2CO_3 solution (2.0 M, 4 mL) and [Pd(PPh$_3$)$_4$] (0.03 g, 0.02 mmol). After refluxing for 20 h, followed by neutralization with hydrochloric acid (0.1 M, 70 mL), products were extracted with dichloromethane (50 mL × 3). The combined organic phase was washed with brine (100 mL), dried over anhydrous $MgSO_4$ and evaporated under reduced pressure. Purification by column chromatography (dichloromethane/*n*-hexane = 1/1 (v/v)), followed by repeated recrystallizations from ethyl acetate/*n*-hexane, afforded **1Cl** as yellow needles (0.08 g, 36%). The obtained yellow needles were further purified by medium-pressure liquid column chromatography (dichloromethane/*n*-hexane = 1/4 (v/v)) and GPC (chloroform with 3 vol%-triethylamine) and evaporated under reduced pressure, affording yellow powder (0.01 g, 4%). R_f = 0.45 (dichloromethane/*n*-hexane = 1/1 (v/v)); m.p. 197.6 °C (decomposition); ^{1}H-NMR ($CDCl_3$): δ = 16.2 (s, 1H, OH), 8.85 (dd, 1H, J = 1.8, 4.6 Hz, 2-Ar–H of HBq), 8.31 (dd, 1H, J = 1.6, 8.0 Hz, 4-Ar–H of HBq), 7.88 (d, 1H, J = 8.8 Hz, 5- or 6-Ar–H of HBq), 7.78 (td, 2H, J = 2.2, 8.8 Hz, Ar–H of ph), 7.65 (s, 1H, 8-Ar–H of HBq), 7.63 (d, 1H, J = 9.2 Hz, 5- or 6-Ar–H of HBq), 7.63 (dd, 1H, J = 4.4, 8.0 Hz, 3-Ar–H of HBq), 7.50–7.43 ppm (m, 6H, Ar–H of ph); HRMS (ESI): calcd for [M + H]$^+$: m/z = 416.0603; found: 416.0583; IR (KBr): $\tilde{\nu}$ = 3423 (OH), 2992 (Ar), 2938 (Ar), 2677 (OH), 1615 (Ar), 1474 (Ar), 1400 (Ar), 1324 (Ar), 1088 (C–Cl), 1011 (Ar), 905 (Ar), 825 (Ar), 812 (Ar), 746 (Ar), 566 (Ar), 540 (Ar), 516 cm^{-1} (Ar).

Synthesis of 7,9-bis(4-trifluoromethylphenyl)-10-hydroxybenzo[*h*]quinoline (1CF$_3$). The reaction was performed similar to the synthesis of **1NMe$_2$** using **HBqI$_2$** (0.23 g, 0.51 mmol), 4-trifluoromethylphenylboronic acid (0.23 g, 1.2 mmol), toluene (9 mL), aqueous Na_2CO_3 solution (1.9 M, 4 mL) and [Pd(PPh$_3$)$_4$] (0.02 g, 0.02 mmol). After refluxing for 45 h, followed by neutralization with hydrochloric acid (0.5 M, 50 mL), products were extracted with dichloromethane (50 mL × 3). The combined organic phase was washed with brine (100 mL), dried over anhydrous $MgSO_4$ and evaporated under reduced pressure. Purification by column chromatography (dichloromethane/*n*-hexane = 3/7 (v/v)), followed by recrystallizations from ethanol twice, afforded **1CF$_3$** as orange needles (0.05 g, 20%). R_f = 0.45 (dichloromethane/*n*-hexane = 3/7 (v/v)); m.p. 183.1–184.4 °C; ^{1}H-NMR ($CDCl_3$): δ = 16.3 (s, 1H, OH), 8.87 (dd, 1H, J = 1.8, 4.6 Hz, 2-Ar–H of HBq), 8.34 (dd, 1H, J = 1.4, 8.2 Hz, 4-Ar–H of HBq), 7.96 (d, 2H, J = 8.0 Hz, Ar–H of ph), 7.89 (d, 1H, J = 9.2 Hz, 5- or 6-Ar–H of HBq), 7.76 (dd. 4H, J = 8.2, 14 Hz, Ar–H of ph), 7.70 (s, 1H, 8-Ar–H of HBq), 7.68 (d, 1H, J = 9.6 Hz, 5- or 6-Ar–H of HBq), 7.66–7.64 ppm (m, 3H; 3-Ar–H of HBq and Ar–H of ph); HRMS (ESI): calcd for [M + H]$^+$: m/z = 484.1131; found: 484.1332; IR (KBr): $\tilde{\nu}$ = 3045 (Ar), 2450 (OH), 1614 (Ar), 1586 (Ar), 1509 (Ar), 1472 (Ar), 1406 (Ar), 1326 (CF$_3$), 1161 (Ar), 1122 (Ar), 1107 (Ar), 1070 (Ar), 1017 (Ar), 920 (Ar), 843 (Ar), 829 (Ar), 777 (Ar), 722 (Ar), 682 cm^{-1} (Ar).

Synthesis of 7,9-bis(4-cyanophenyl)-10-hydroxybenzo[*h*]quinoline (1CN). The reaction was performed similar to the synthesis of **1NMe$_2$** using **HBqI$_2$** (0.19 g, 0.43 mmol), 4-cyanophenylboronic acid (0.15 g, 1.0 mmol), *N*,*N*-dimethylformamide (DMF, 7 mL), aqueous Na_2CO_3 solution (1.9 M, 3 mL) and [Pd(PPh$_3$)$_4$] (0.02 g, 0.02 mmol). After refluxing for 48 h, followed by neutralization with hydrochloric acid (2 mL) and aqueous $NaHCO_3$ solution (8 mL), the products were extracted with dichloromethane (40 mL × 3). The combined organic phase was washed with brine (100 mL), dried over anhydrous $MgSO_4$ and evaporated under reduced pressure. Purification by

column chromatography (dichloromethane/*n*-hexane = 5/1 (v/v)), followed by repeated recrystallizations from acetonitrile, afforded **1CN** as orange needles (0.05 g, 31%). R_f = 0.20 (dichloromethane/*n*-hexane = 5/1 (v/v)); m.p. 268.1–269.6 °C; ^{1}H-NMR ($CDCl_3$): δ = 16.5 (s, 1H, OH), 8.88 (dd, 1H, J = 1.6, 4.8 Hz, 2-Ar–H of HBq), 8.36 (dd, 1H, J = 1.6, 8.0 Hz, 4-Ar–H of HBq), 7.97 (td, 2H, J = 1.9, 8.7 Hz, Ar–H of ph), 7.84 (d, 1H, J = 9.2 Hz, 5 or 6-Ar–H of HBq), 7.82 (td, 2H, J = 1.9, 8.3 Hz, Ar–H of ph), 7.78 (td, 2H, J = 1.8, 8.6 Hz, Ar–H of ph), 7.71 (d, 1H, J = 9.2 Hz, 5 or 6-Ar–H of HBq), 7.69 (dd, 1H, J = 5.0, 8.2 Hz, 3-Ar–H of HBq), 7.66 (s, 1H, 8-Ar–H of HBq), 7.64 ppm (td, 2H, J = 2.0, 8.4 Hz, Ar–H of ph); HRMS (ESI): calcd for $[M + H]^+$: m/z = 398.1288; found: 398.1276; IR (KBr): $\tilde{\nu}$ = 3080 (Ar), 3036 (Ar), 2520 (OH), 2231 (CN), 1604 (Ar), 1515 (Ar), 1472 (Ar), 1428 (Ar), 1405 (Ar), 1328 (Ar), 1308 (Ar), 1197 (Ar), 1120 (Ar), 902 (Ar), 835 (Ar), 828 (Ar), 773 (Ar), 706 (Ar), 621 (Ar), 556 (Ar), 542 cm^{-1} (Ar).

Synthesis of 7,9-bis(4-nitrophenyl)-10-hydroxybenzo[*h*]quinoline (1NO$_2$). The reaction was performed similar to the synthesis of **1NMe$_2$** using **HBqI$_2$** (0.25 g, 0.56 mmol), 4-nitrophenylboronic acid (0.23 g, 1.4 mmol), toluene (8 mL), ethanol (3 mL), aqueous Na_2CO_3 solution (2.2 M, 4 mL) and $[Pd(PPh_3)_4]$ (0.02 g, 0.02 mmol). After refluxing for 70 h, followed by neutralization with hydrochloric acid (0.2 M, 100 mL), the products were extracted with dichloromethane (50 mL × 3). The combined organic phase was washed with brine (100 mL), dried over anhydrous $MgSO_4$ and evaporated under reduced pressure. Purification by column chromatography (dichloromethane/*n*-hexane = 7/3 (v/v)), followed by washing with dichloromethane/*n*-hexane = 1/1 (v/v) (20 mL), afforded **1NO$_2$** as an orange powder (0.07 g, 27%). R_f = 0.45 (dichloromethane/*n*-hexane = 7/3 (v/v)); m.p. 285.0–287.0 °C; ^{1}H-NMR ($CDCl_3$): δ = 16.6 (s, 1H, OH), 8.91 (dd, 1H, J = 1.4, 4.6 Hz, 2-Ar–H of HBq), 8.41–8.35 (m, 5H, Ar–H of ph and 4-Ar–H of HBq), 8.04 (td, 2H, J = 2.3, 9.3 Hz, Ar–H of ph), 7.87 (d, 1H, J = 9.2 Hz, 5- or 6-Ar–H of HBq), 7.72 (s, 1H, 8-Ar–H of HBq) 7.75–7.69 (m, 3H, 3-Ar–H of HBq and Ar–H of ph), 7.71 ppm (d, 1H, J = 8.8 Hz, 5- or 6-Ar–H of HBq); HRMS (ESI): calcd for $[M + H]^+$: m/z = 438.1084; found: 438.1068; IR (KBr): $\tilde{\nu}$ = 3106 (Ar), 3080 (Ar), 2445 (OH), 1590 (Ar), 1510 (NO_2), 1344 (NO_2), 1126 (Ar), 1110 (Ar), 856 (Ar), 841 (Ar), 734 cm^{-1} (Ar).

Deuteration of the hydroxy group in 1Me and 1NO$_2$. Hydroxy groups in **1Me** and **1NO$_2$** were not deuterated upon cycles of dissolution in CD_3OD and evaporation, although the hydrogen in HBq was successfully deuterated as reported by Joo and coworkers.[37] The results are reasonable since the hydroxy groups in 1R are more strongly bound to the imine nitrogen in benzo[*h*]quinoline moieties than that in HBq as their ^{1}H-NMR signals are observed in the low-field region (Fig. S2 and S5–S13; δ_{O-H} = 16.0 ppm for **1Me**, 16.6 ppm for **1NO$_2$** and 14.9 ppm for HBq). Thus, the hydroxy groups of the derivatives were deuterated by employing the acid–base reaction. **1Me** or **1NO$_2$** was added to a suspension of potassium hydroxide (>0.23 g, >4.1 mmol) in 1,4-dioxane (2 mL). After stirring at room temperature overnight, the reaction mixture was neutralized by adding acetic acid-d_4, evaporated and dried under vacuum. On the basis of the ^{1}H-NMR spectra (Fig. S14 and S15), 39 and 30% of hydroxy groups of **1Me** and **1NO$_2$** were deuterated, respectively.

Spectroscopic and photophysical measurements

HBq, purchased from Ambeed, Inc., was purified by recrystallization from *n*-hexane.[38] Dichloromethane for fluorometry (KANTO CHEMICAL Co., Inc), ethyl acetate, acetone, DMF for spectroscopy (FUJIFILM Wako Pure Chemical Corporation), HPLC-grade acetonitrile (Merck Millipore) and trifluoroacetic acid for HPLC/Spectro grade (TFA, Thermo Fisher Scientific) were used without purification.

Absorption spectra of the derivatives were measured using a Hitachi High-Technologies U-3900 spectrophotometer (slit width: 1 nm, scan speed: 120 nm min^{-1}). Fluorescence spectra were obtained, and the Φ_f values were determined using a Hamamatsu Photonics Quantaurus-QY Plus C13534-02 (excitation wavelength: 375–415 nm, averaging: 1000-(without TFA) or 200-times (with TFA)). In fluorescence decay measurements, a second harmonic femtosecond-pulsed Ti : sapphire laser (395 nm, 1 MHz) from MKS Instruments Spectra-Physics Tsunami® 3941-M1BB oscillator with 3980 or GWU-UHG-2PSK-W pulse picker/frequency doubler was used as an excitation light. Fluorescence from the sample was detected by a Hamamatsu Photonics C4334 streak camera equipped with a C5094 spectrograph. The fluorescence decay profiles were successfully fitted using a single-exponential decay function by convoluting the instrumental response function obtained as the excitation-light scattering by colloidal silica LUDOX® HS-30 (Sigma-Aldrich Co. LLC). All the spectroscopic and photophysical data were analyzed using OriginPro 2023 software.

^{1}H-NMR titration for the addition of trifluoroacetic acid

$CDCl_3$ was employed as the solvent by considering the solubilities of derivatives. Reagents and ^{1}H-NMR measurement conditions are the same as those described above. A solution of TFA in $CDCl_3$ (100 mM, each 0.010 mL) was added 10 times to solutions of 1R (R = –OMe to –NO_2) in $CDCl_3$ (1.00 mL). For **1NMe$_2$**, $CDCl_3$ solutions of TFA with concentrations of 20, 100 and 1000 mM were used. Concentrations of 1R before the TFA addition were ~5 mM for the derivatives, except for **1NO$_2$** and 4.3 mM for **1NO$_2$**. Low concentration of **1NO$_2$** is due to its low solubility in $CDCl_3$.

Theoretical calculations

The calculations were performed using Gaussian 16W (Revision A.03).[39] Ground-state geometries of a molecule or its protonated ion were optimized by using the B3LYP[40] functional with the 6-311+G(d,p)[41] basis set unless otherwise specified. Two steric structures with different relative dihedral orientations of the 4-Rphenyl groups were optimized, and the one with a lower Gibbs energy was used for subsequent calculations. It should be noted that two optimized steric structures of the present derivatives possess comparable Gibbs energies. The TD-DFT calculations were conducted to estimate the energies and oscillator strengths of the 30 lowest-energy singlet absorption transitions. Excited-state geometries of a molecule or ion were optimized by the TD-DFT method under the B3LYP/6-31G(d,p) level, and then, the transition energies and oscillator strengths to give the

3 lowest-energy singlet and triplet excited states were calculated under the B3LYP/6-311+G(d,p) level. No connectivity was specified in the calculations. Dichloromethane or acetonitrile was considered as a solvent by using a conductor-like polarizable continuum model (CPCM).[42] The Kohn–Sham molecular orbitals were visualized using GaussView 6.0.16.[43]

Results and discussion

Crystal structures and ground-state optimized geometries

Thermal recrystallizations of 1R (R = –NMe_2, –OMe, –Me, –H, –F, –CF_3) from acetonitrile, ethanol or ethyl acetate/*n*-hexane gave single-crystal samples suitable for X-ray crystallographic analyses. Crystal structures and crystallographic data are shown in Fig. S16–S21 and Tables S1 and S2, respectively. Some compounds contained a disordered component in which the HBq moiety was flipped, and therefore, all the crystal structures were not necessarily solved in very good quality. All the C–O lengths at the 10-position of the HBq moieties (Table S3) were larger than 1.35 Å. Although hydrogen atoms are not experimentally observable in the crystallographic analysis, the C–O lengths comparable to that of 1-naphthol in the crystalline phase (1.376(2) Å)[44] strongly suggest that the molecules in the ground states are enol forms. Dihedral angles between the HBq moiety and 4-Rphenyl groups were determined to be ±40–±58° and ±23–±47° at the 7- and 9-positions, respectively (Table S3). The variations of the dihedral angles are presumably due to molecular packing in the crystalline phases. To compare the structures of 1R without the effects of packing, the ground-state geometries of the molecules were optimized by DFT calculations. The optimized geometries in Fig. S22 agreed with the structures obtained from crystallographic analyses. All the derivatives adopted enol forms with an intramolecular hydrogen bond, although no bond connectivity was specified in the optimization process. Upon decreasing the electron-donating ability, followed by increasing the electron-withdrawing ability of the substituent R, both C–O and N···H lengths slightly decreased (*e.g.*, 1.351 Å (C–O) and 1.633 Å (N–H) for **1NMe$_2$**, 1.342 Å (C–O) and 1.614 Å (N–H) for **1NO$_2$**) with an increase in the O–H length (*e.g.*, 1.003 and 1.009 Å for **1NMe$_2$** and **1NO$_2$**, respectively): see Table S4. The trend is explainable by a decrease in electron density at the oxygen atom and consistent with the downfield shift of the O–H signal in the ^{1}H-NMR spectra of 1R in $CDCl_3$ (Fig. S5–S13; δ_{O-H} = 15.9 and 16.6 ppm for **1NMe$_2$** and **1NO$_2$**, respectively). The absolute values of dihedral angles between the HBq moiety and the 4-Rphenyl groups were determined to be 54–60° and 42–46° at the 7- and 9-positions, respectively, irrespective of the substituent R. The results indicate that the spectroscopic and photophysical properties of 1R are best characterized by the electron-donating/-withdrawing nature of the substituent R.

Absorption spectra in dichloromethane

Fig. 1 shows the absorption spectra of 1R in dichloromethane at room temperature, along with that of HBq. Spectroscopic properties of 1R are summarized in Table 1. All the derivatives exhibited multiple absorption bands in the measured

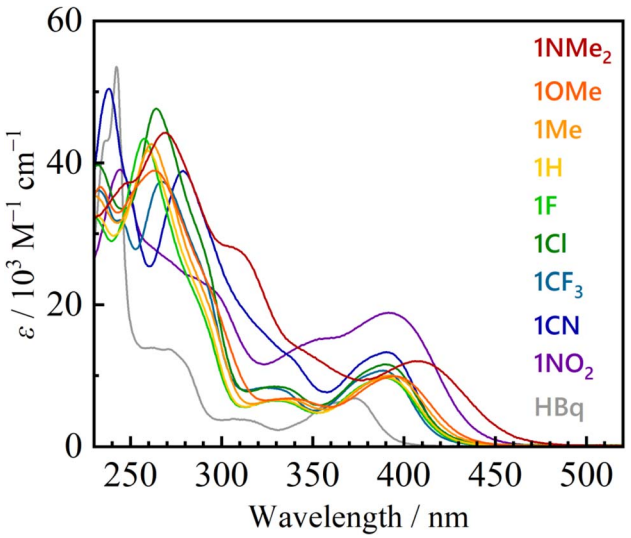

Fig. 1 Absorption spectra of 1R and HBq in dichloromethane at room temperature.

wavelength region, and the lowest-energy absorption band was observed at around 400 nm. The bands were of lower energy than that of HBq, reflecting the extended π-system arising from the electronic interactions between the HBq moiety and 4-Rphenyl groups at the 7- and 9-positions. Since the energy and intensity of the lowest-energy band of 1R were varied by varying the substituent R, we evaluated the band by accounting for the Hammett substituent constant at the *para* position (σ_p). The value is determined by the acidity index (pK_a) of 4-substituted benzoic acid relative to that of benzoic acid and is a measure of the electron-donating/-withdrawing ability of the substituent.[31] Fig. 2 shows plots for the maximum wavenumber ($\tilde{\nu}_a$) and the molar absorption coefficient (ε_{max}) of the lowest-energy band of 1R against the σ_p value. The band of **1NMe$_2$** was observed at the lowest energy among the present derivatives, and the energy increased with a decrease in the electron-donating ability of the substituent, accompanied by a decrease in the molar absorption coefficient. The behavior can be explained as follows. The presence of strong electron-donating dimethylamino groups extends the charge-transfer interaction in the HBq moiety, and the transition dipole moment decreases upon decreasing the electron-donating ability of the substituent. On the other hand, when strong electron-withdrawing substituents were introduced, the band exhibited the opposite trend: low-energy shift and enhancement upon increasing the electron-withdrawing ability of the substituent. The results indicate a contribution(s) of another electronic transition(s) to the lowest-energy transition of the derivatives with the electron-withdrawing groups. To investigate the electronic transitions of the derivatives, TD-DFT calculations were performed. The calculated excited states are summarized in Tables S5–S13. As the calculated electronic transitions sufficiently agree with the observed absorption spectra within the accepted error of transition energies (<10%, see Fig. S23), our TD-DFT calculations reproduce the present molecules well. The lowest-energy singlet excited (S_1) states of the derivatives except for **1NO$_2$** are best

Table 1 Spectroscopic and photophysical properties of 1R in dichloromethane at room temperature

Derivative	λ_{abs}/nm (ε/10^4 M^{-1} cm^{-1})	λ_{fl}[a]/nm	Φ_f[a]	τ_f[b]/ns	k_f[c]/10^7 s^{-1}	k_d[c]/10^9 s^{-1}
1NMe$_2$	246 (3.68), 269 (4.42), 310 (2.76), 409 (1.20)	750	0.004	0.046	8.4	22
1OMe	234 (3.66), 264 (3.89), 339 (0.68), 395 (0.98)	695	0.007	0.10	6.9	9.9
1Me	231 (3.53), 262 (4.62), 333 (0.67), 393 (1.00)	687	0.007	0.17	4.0	5.8
1H	231 (3.25), 260 (4.17), 331 (0.66), 390 (1.01)	680	0.01	0.17	6.3	5.7
1F	229 (3.26), 257 (4.34), 331 (0.65), 390 (0.97)	678	0.01	0.18	6.4	5.6
1Cl	232 (3.97), 264 (4.76), 329 (0.85), 390 (1.02)	668	0.01	0.19	6.1	5.2
1CF$_3$	233 (3.61), 267 (3.73), 325 (0.83), 389 (1.07)	663	0.02	0.28	8.1	3.5
1CN	238 (5.04), 280 (3.87), 337 (1.28), 390 (1.02)	657	0.02	0.37	6.3	2.6
1NO$_2$	244 (3.90), 293 (2.26), 350 (1.49), 392 (1.89)	651	0.02	0.21	8.0	4.8

[a] λ_{ex} = 375–415 nm. [b] λ_{ex} = 395 nm. [c] $\Phi_f = k_f\tau_f = k_f/(k_f + k_d)$.

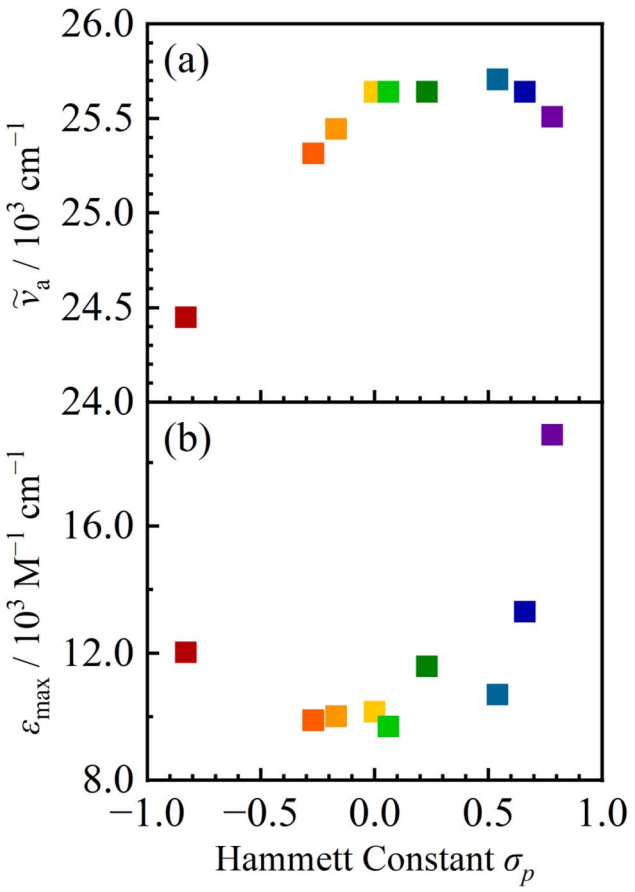

Fig. 2 Dependences of σ_p on the absorption maximum wavenumber (a) and the corresponding molar absorption coefficient (b) of the lowest-energy band of 1R in dichloromethane. The colors correspond to those indicated in Fig. 1.

characterized by the HOMO → LUMO transitions. The Kohn–Sham orbitals corresponding to the S_1 states of 1R are shown in Fig. 3. Their S_1 states belong to the ππ* transition with a small contribution of charge-transfer character in the HBq moiety. The distribution of the HOMO has extended to the 4-Rphenyl groups as the electron-donating ability of the substituent R increased. This result indicates that the introduction of electron-donating substituents, such as dimethylamino groups, increases the contribution of ground-state orbitals, leading to an enhanced charge-transfer character of the HBq moiety as expected above. The absorption band generally shifts to longer wavelength with increasing charge-transfer characteristics, and an increase in the transition dipole moment results in an increase in the molar absorption coefficient, which is consistent with the present experimental results. On the other hand, the 4-Rphenyl groups with the electron-withdrawing substituents have contributed to the LUMO of a derivative and reduce the charge-transfer character in the HBq moiety. Especially, the lowest-energy absorption transition of **1NO$_2$**, having the strongest electron-withdrawing nitro group, corresponded to the HOMO → LUMO (69%)/LUMO + 1 (31%) transition, where the LUMOs were localized exclusively on the 4-nitrophenyl groups. The lowest-energy transition of **1NO$_2$** is, thus, ascribed to a charge-transfer transition from the HBq moiety to the 4-nitrophenyl groups. To understand the excited-state switching behavior obtained for **1NO$_2$**, we examined the TD-DFT results in detail (Fig. S24). As described above, the charge-transfer excited states in the HBq moiety were obtained as the S_1 state for the derivatives except for **1NO$_2$**, and the transition energy increased with increasing σ_p. An excited state with similar electronic character was also found for **1NO$_2$** as the upper-lying excited (S_3) state. Meanwhile, the excited state ascribed to the charge-transfer from the HBq moiety to the 4-Rphenyl group at the 7-position, which was obtained as the S_1 state for **1NO$_2$**, was upper-lying for the other derivatives, and the transition energy

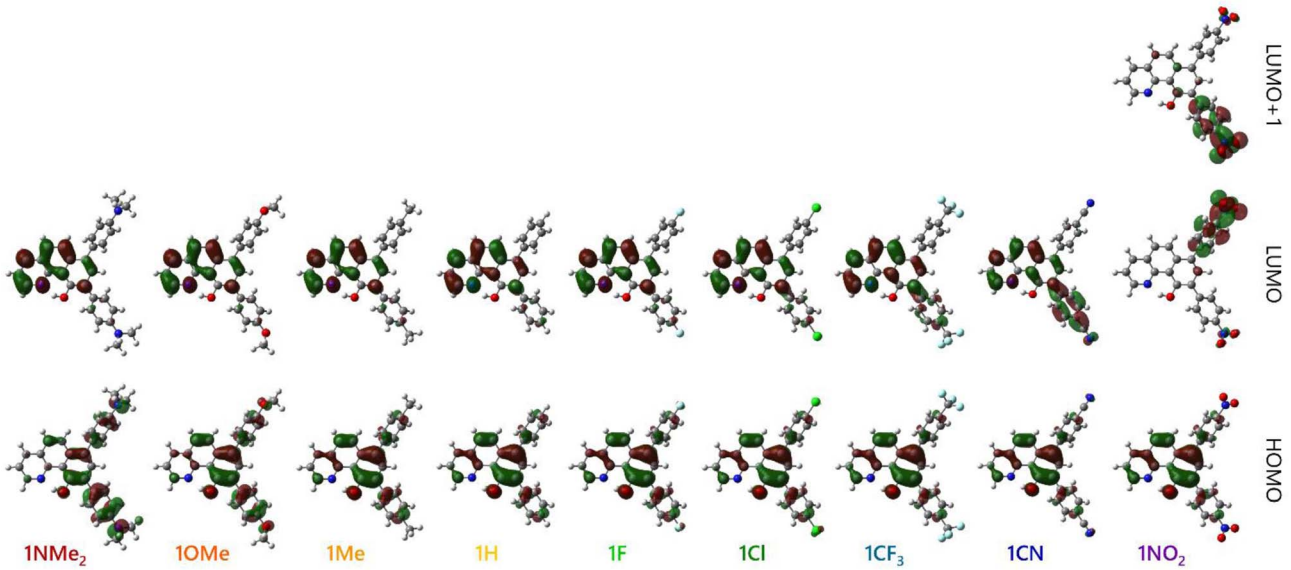

Fig. 3 Kohn–Sham orbitals relating to the S_1 states of 1R in dichloromethane.

increased with decreasing σ_p (not found in the S_1–S_{30} states of **1NMe$_2$**). As a result of the σ_p dependences of two charge-transfer excited states, the electronic character of **1NO$_2$** with the strongest electron-withdrawing group was switched with those of the other 1R. Such a difference in the electronic structures of the lowest-energy excited states of 1R is expected to affect the fluorescence behavior of the derivatives.

Fluorescence properties in dichloromethane

All the derivatives exhibited orange–red fluorescence in diluted solutions. Fig. 4(a) shows the fluorescence spectra of 1R and HBq in dichloromethane at room temperature, and their fluorescence characteristics are summarized in Table 1. The intensities of the fluorescence spectra are scaled so that the integration of the spectrum in the wavenumber scale corresponds to the fluorescence quantum yield. The spectral band shape of 1R was broad/structureless and much lower in energy than the absorption band ($\Delta\tilde{\nu} > 10\,000$ cm^{-1}), irrespective of the derivatives. Since these characteristics originate from large excited-state reorganization, the fluorescence of 1R seems to be from the keto forms generated by intramolecular proton transfer. The fluorescence energy monotonically increased with increasing σ_p as shown in Fig. S25(a), whereas the absorption energy decreased in the order of **1CF$_3$** ($\sigma_p = +0.54$), **1CN** ($\sigma_p = +0.66$), **1NO$_2$** ($\sigma_p = +0.78$), and the TD-DFT calculation assigned the S_1 state of **1NO$_2$** to the charge transfer from the HBq moiety to the 4-nitrophenyl group, which appears free from the proton-transfer process. To explain such differences between absorption (excitation) and fluorescence processes, either excited-state switching owing to large reorganization energy upon the proton transfer process or the presence of another excited-state stabilization process with a reorganization energy comparable to that of the proton transfer is required. As indicating the latter contribution, in contrast to the spectral similarity, the photophysical properties of **1NO$_2$** did not follow the trend of the other derivatives. Although the fluorescence quantum yield (Φ_f) and fluorescence lifetime (τ_f) increased with an increase in the fluorescence energy and σ_p, fluorescence from **1NO$_2$** ($\Phi_f = 0.02$ and $\tau_f = 0.21$ ns) was weaker and shorter-lived than that from **1CN** ($\Phi_f = 0.03$ and $\tau_f = 0.37$ ns). The results indicate that the fluorescence and/or nonfluorescence processes of **1NO$_2$** are different from those of the other derivatives. The fluorescence rate constant (k_f) varied by up to 2.1-fold among the derivatives (4.0×10^7 s^{-1} for **1Me** and 8.4×10^7 s^{-1} for **1NMe$_2$**, see Table 1 and Fig. S25(b)). Although the difference in k_f suggests successful tuning of the electronic structures of 1R by varying the substituent R, the trend is not clear among the present derivatives. On the other hand, the nonfluorescence rate constant (k_d) exhibited an obvious fluorescence-energy dependence. As shown in Fig. 4(b), ln k_d of 1R except for **1NO$_2$** linearly decreased with increasing the fluorescence maximum wavenumber $\tilde{\nu}_f$, as expressed by the energy gap law.[45–47] The k_d value for **1NO$_2$** was, however, larger than that expected from the fluorescence energy. In practice, the coefficient of determination for the linear regression for all the derivatives ($R^2 = 0.89361$) was worse than that for the derivatives without **1NO$_2$** ($R^2 = 0.94690$). We recently reported fluorescent solvatochromic derivatives with a 4-nitrophenyl group (*i.e.*, 1-methoxy-4-(4-nitrophenyl)naphthalene and its relatives) and their nonfluorescent pathways.[48] The charge-transfer excited states of the derivatives have exhibited the V-shape energy gap dependence of ln k_d, and it deactivates *via* the internal conversion to the ground state when the fluorescence energy of the derivative is smaller than 17 000 cm^{-1}. The k_d value of **1NO$_2$**, whose partial structure is comparable to 1-methoxy-4-(4-nitrophenyl) naphthalene, obeys the energy gap plots for derivatives with a 4-nitrophenyl group (see Fig. S26). It strongly suggests that fluorescence from **1NO$_2$** originates from the charge-transfer transition to the 4-nitrophenyl group rather than the keto form generated by ESIPT. The low-energy fluorescence from

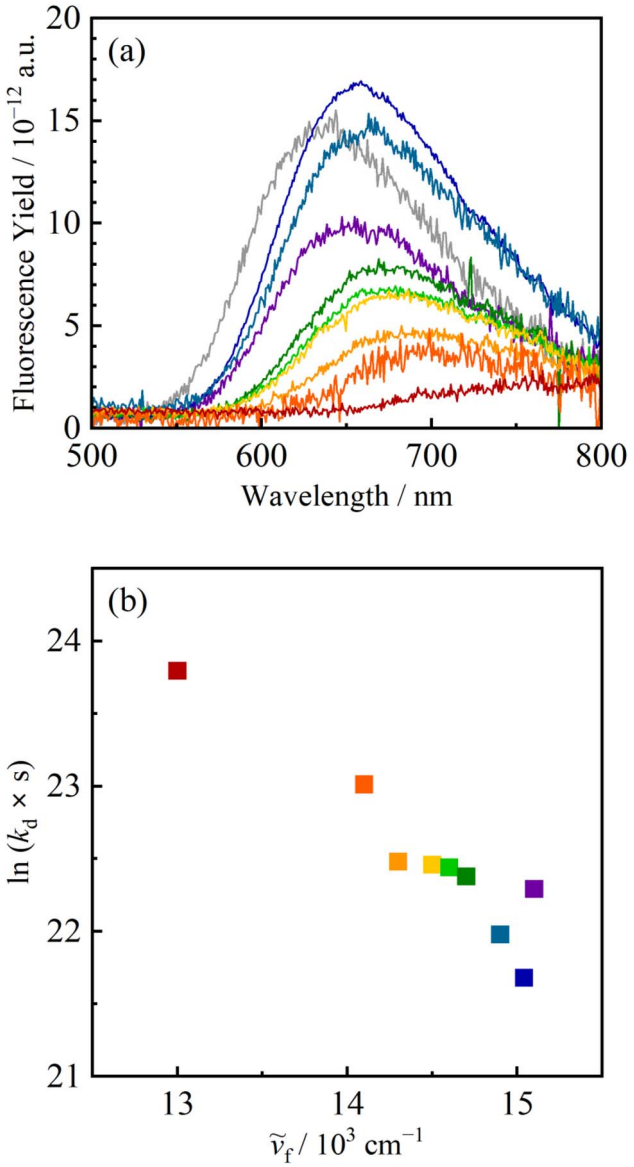

Fig. 4 (a) Fluorescence spectra (λ_{ex} = 375–415 nm) and (b) energy gap plots of 1R in dichloromethane at room temperature. The grey curve in (a) represents a spectrum of HBq in dichloromethane at room temperature. The colors correspond to those indicated in Fig. 1.

1NO$_2$ can be explained by the large stabilization of its charge-transfer excited state with a large electric dipole moment due to solvation. The charge-transfer character of the excited state of **1NO$_2$** was also suggested by comparing with the fluorescence properties in the crystalline phase. The derivatives exhibited more intense fluorescence in the crystalline phases (Fig. S27 and Table S14) than in dichloromethane. The intense fluorescence originates from 1.6–4.1-times smaller k_d for the derivatives except for **1NO$_2$**. In contrast, the k_d value of **1NO$_2$** in the crystalline phase was 7.2-times smaller than that in dichloromethane. The results indicate the impact of solvation on the excited-state dynamics of **1NO$_2$**.

Geometries of 1R in the S_1 states were optimized by the TD-DFT method (Fig. 5 and S28), and excited states in the S_1-optimized geometries were calculated (in Tables S15–S23). The derivatives, except for **1NO$_2$**, possessed the keto form generated by ESIPT. On the other hand, in **1NO$_2$**, the 4-nitrophenyl group at the 7-position was perpendicularly oriented to the HBq moiety (dihedral angle being 89.76°). Such differences in the excited-state geometry are considered to originate from a change in the charge distribution associated with photoexcitation. The ESIPT process is driven by the charge-transfer transition in the HBq moiety, upon which charge distributions on the photoacidic oxygen atom decrease and that on the photobasic imine nitrogen atom increases. Thus, the charge transfer from the HBq moiety to the 4-nitrophenyl group without the charge distribution change on the nitrogen atom did not induce the proton-transfer process in **1NO$_2$**. In practice, the Gibbs energy of the S_1 state of **1NO$_2$** as a function of the O–H distance possessed a local minimum at ~1.1 Å, which corresponds to the non-ESIPT geometry, with an activation energy toward the proton-transfer pathway being ~0.05 eV (see Fig. S29) in contrast to other derivatives including HBq without any activation barrier (Fig. S3). The difference in the excited-state character of **1NO$_2$** is also observed as the solvent dependence of the fluorescence spectra (see Fig. S30 and Table S24). Although typical ESIPT-type fluorescence from an HBq derivative is insensitive to solvents, **1NO$_2$** showed significant fluorescence quenching with increasing solvent polarity. We note that the k_d values increased upon ~30% deuteration of the hydroxy groups in **1Me** and **1NO$_2$** by a factor of ~1.3 (Fig. S31 and Table S25) and that differences in the spectroscopic and photophysical characteristics between the derivatives are not clear at this stage. Joo and coworkers have reported that the proton transfer occurs in 12 ± 6 and 25 ± 5 fs in HBq and its deuterated derivative, respectively.[37] The time scale is much faster than that of the fluorescence lifetime in the present study (>45 ps), and therefore, a significant difference might not be observed between ESIPT-type **1Me** and non-ESIPT-type **1NO$_2$**.

TFA addition in acetonitrile

The introductions of 4-Rphenyl groups into the HBq skeleton successfully controlled the electronic structures of the derivatives and resulted in a change in the charge-transfer character in its electronic transition. The results support our expectation that the ESIPT process of an HBq derivative corresponds to an intramolecular acid–base reaction, and therefore, it is expected that the addition of external acid also affects the spectroscopic/photophysical properties of the derivatives. Fig. 6 and S32–S39 show the absorption and fluorescence spectra of 1R in the absence and presence of trifluoroacetic acid (TFA). Acetonitrile was employed as the solvent by considering the solubility of the protonated form of 1R. The absorption spectra of 1R (R = –OMe to –CN) responded to the presence of TFA by exhibiting multiple isosbestic points, and the lowest-energy absorption bands were lowered in energy and weakened compared to those of the corresponding 1R. Furthermore, strong fluorescence appeared at a shorter wavelength with reduced fluorescence from the keto form upon the addition of TFA. These spectral changes are explainable by protonation of the imine nitrogen atom, which

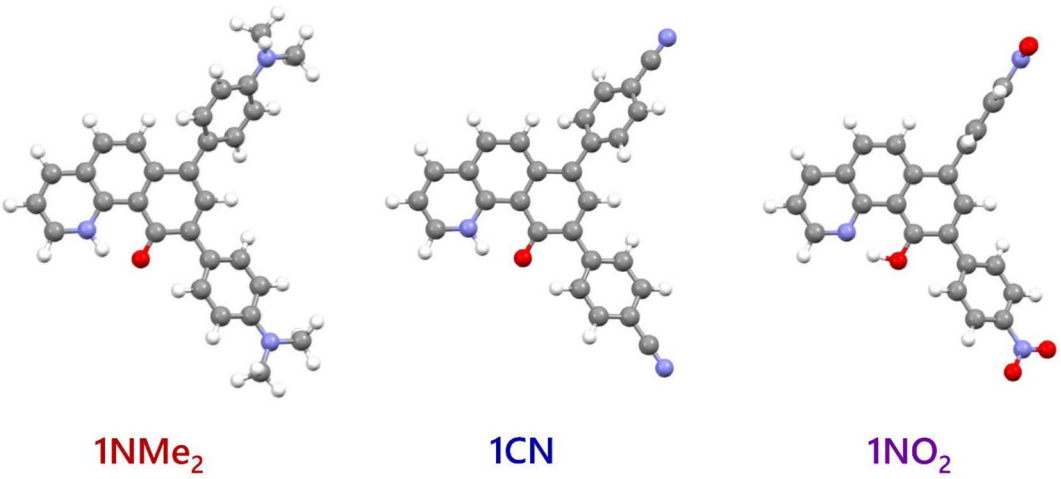

Fig. 5 Optimized geometries of **1NMe$_2$**, **1CN** and **1NO$_2$** in the S_1 states in dichloromethane.

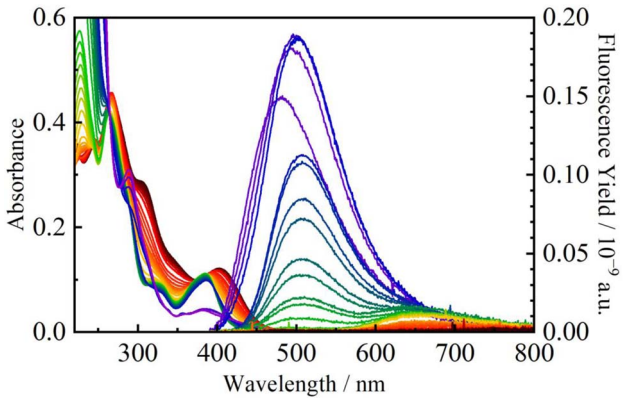

Fig. 6 Absorption and fluorescence spectra (λ_{ex} = 375 nm) of **1NMe$_2$** (1.02×10^{-5} M) in the absence and presence of TFA (0–500 mM, dark red → purple) in acetonitrile.

suppresses the ESIPT process. On the other hand, while the absorption spectral change of **1NO$_2$** was not large, it exhibited an isosbestic point at around 400 nm and the lowest-energy band was weakened. Weak fluorescence from **1NO$_2$** in high-polar acetonitrile was further reduced, and a new weak fluorescence appeared at around 500 nm upon the addition of TFA. As discussed above, the excited state of **1NO$_2$** is not ESIPT-type, and therefore, the spectroscopic changes upon TFA addition correspond to the reduced charge-transfer character by a decrease in the electron density of the oxygen atom in the hydroxy group with an additional hydrogen bond. Both absorption and fluorescence spectra of **1NMe$_2$** with the Brønsted-basic dimethylamino groups significantly changed over a wide range of TFA concentration (0–500 mM, see Fig. 6). Fluorescence color changed over a broad visible region as a function of TFA concentration. The absence of the isosbestic point suggests that the spectroscopic changes result from multistep reactions in which the two dimethylamino groups and the HBq moiety are protonated. In practice, in the low-concentration region ([TFA] = 0–100 μM), isosbestic points were obtained at 392, 378 and 271 nm, which is considered to reflect the first protonation step. In the [TFA] = 0.2–10 mM region, a high-energy absorption band at ~380 nm and fluorescence band at around 650 nm were observed. Since these bands closely matched those of **1CF$_3$** in acetonitrile, the spectral features originate from an HBq derivative having the "electron-withdrawing" dimethylammonio (-NMe$_2$H$^+$) groups. Upon further TFA addition, fluorescence from the keto form disappeared, and new intense greenish-blue fluorescence was observed in the shorter-wavelength region. The band arises from **1NMe$_2$**·3H$^+$, in which the two dimethylamino groups and the HBq moiety are protonated. To investigate the details of the protonation processes of 1R, we conducted DFT calculations. Adequacies of the calculations in acetonitrile were confirmed by comparing the TD-DFT results and the experimentally-observed absorption spectra of 1R in the absence and presence of TFA (Tables S27–S46 and Fig. S43–S45). In the optimized ground-state geometries of 1R·H$^+$ (**1NMe$_2$**·3H$^+$ in the case of **1NMe$_2$**), both oxygen and nitrogen atoms in the HBq moiety were protonated, as shown in Fig. S41. The protonation of the proton-accepting moiety precludes ESIPT and yields non-ESIPT high-energy fluorescence (Tables S47–S66). Comparisons of the Gibbs energies for various protonated states of **1NMe$_2$** revealed that protonation occurs in the order of the dimethylamino group at the 9-position, the dimethylamino group at the 7-position, and the HBq moiety.

Basicity indices (pK_b) of 1R (R = –OMe to –NO$_2$) were evaluated by titration analyses for the absorption spectra and single-step equilibrium process: 1R + CF$_3$COOH ⇄ 1R·H$^+$ + CF$_3$COO$^-$. Global fits for the absorbance (A_{obs}) changes at the multiple wavelengths against the TFA concentrations using eqn (1) successfully provided the pK_b values of 1R (Fig. S32–S39).

$$A_{obs} = \frac{A_0 + A_1 10^{-pK_b}[TFA]}{1 + 10^{-pK_b}[TFA]} \quad (1)$$

where A_0 and A_1 are the absorbances of 1R and 1R·H$^+$ at the concentration of [1R], respectively. The pK_b value of the ESIPT-type 1R increased with increasing σ_p of the substituent R. The

trend can be explained by a decrease in the electron density on the hydroxy oxygen atom by the electronic nature of the substituent. The results are consistent with the downfield-shifted O–H signal in the ^{1}H-NMR data and qualitatively reproduced by DFT calculations (estimated by an equation $K_b = \exp(-\Delta G_{tot}/k_B T)$ where ΔG_{tot}, k_B and T are the calculated Gibbs energy difference, Boltzmann constant and absolute temperature (298.15 K), respectively, see Table S26 and Fig. S42). The pK_b value of **1NO$_2$** was extremely low (-3.21 ± 0.21) compared with the other derivatives, despite the strong electron-withdrawing ability of the nitro group. Although we performed calculations for an acinitro species, the experimental result could not be reproduced. The protonation of the derivatives was also traced by ^{1}H-NMR spectroscopy (Fig. S49–S56). The signal from the 2-position of the benzo[*h*]quinoline moiety shifted to the downfield upon the addition of TFA (Fig. S57), and changes in the chemical shifts of the derivatives with the electron-donating groups (*e.g.*, **1OMe**) started by adding 1-mM TFA, whereas those with the electron-withdrawing groups (*e.g.*, **1CN**) required higher concentration (~5 mM or more).

The three-step protonation process of **1NMe$_2$** was treated as three successive equilibrium processes, and the absorbance changes under [TFA] = 0–100 mM were globally fitted using eqn (2).

$$A_{obs} = \frac{A_0 + A_1 10^{-pK_{b1}}[TFA] + A_2 10^{-pK_{b1}-pK_{b2}}[TFA]^2 + A_3 10^{-pK_{b1}-pK_{b2}-pK_{b3}}[TFA]^3}{1 + 10^{-pK_{b1}}[TFA] + 10^{-pK_{b1}-pK_{b2}}[TFA]^2 + 10^{-pK_{b1}-pK_{b2}-pK_{b3}}[TFA]^3} \quad (2)$$

As shown in Fig. S40, the absorbance changes upon the TFA addition were well reproduced by three successive protonation models, and the first two protonation processes possess small pK_a values below −3, as expected from the strongly basic dimethylamino group. In the ^{1}H-NMR titration experiments (Fig. S46–S48), the change in the chemical shift was completed at 10-mM TFA, suggesting quantitative two-protonation of the dimethylamino groups, and further change, which is ascribed to the protonation of the hydroxy group, occurred at the <70-mM region (Fig. S57). These TFA-addition experiments to 1R demonstrate that the basicity of a derivative can be controlled by the electronic nature of the substituent R introduced into the HBq skeleton. In particular, **1NMe$_2$**, whose substituent itself possesses proton-accepting ability, achieved color-tunable fluorescence over the near-infrared to blue region.

Conclusions

The charge-transfer character in electronic transitions and excited-state geometry of the 10-hydroxybenzo[*h*]quinoline (HBq) skeleton was successfully tuned through the electronic nature of substituents. Single-crystal X-ray analyses and DFT calculations suggested that the HBq derivatives with nine different R substituents at the 7- and 9-positions (1R; R = –NMe$_2$, –OMe, –Me, –H, –F, –Cl, –CF$_3$, –Cl, –CN, –NO$_2$) in the ground states are enol forms with an intramolecular hydrogen bond. All the derivatives exhibited an obvious visible absorption band at ~400 nm and orange–red fluorescence in dichloromethane at room temperature. The fluorescence from 1R (R = –NMe$_2$ to –CN) was best characterized as the excited-state intramolecular proton transfer (ESIPT) upon charge-transfer transition in the HBq moiety, and the charge-transfer character was controlled by the electron-donating/-withdrawing ability of the substituent R. In contrast, the spectroscopic and photophysical features of **1NO$_2$** with the strongest electron-withdrawing nitro groups were largely different from those of other derivatives. The S_1 transition of **1NO$_2$** was ascribed to the charge transfer from the HBq moiety to the 4-nitrophenyl group. Reflecting such a difference in the electronic transition, **1NO$_2$** emits from the non-ESIPT excited state, which is stabilized by solvation and twisting the 4-nitrophenyl group. These findings demonstrate that the electronic nature of the substituent induces distinct excited-state structural changes even for the same skeleton and that changes in the charge distributions at both the proton-donating and -accepting moieties upon photoexcitation are crucial for the ESIPT process. The excited-state structure of 1R was varied by adding trifluoroacetic acid, resulting in intense fluorescence from the non-ESIPT excited states of their protonated form. The introduction of the 4-Rphenyl groups modified the basicity and acid–base behavior of the HBq skeleton. Notably, **1NMe$_2$** possessing proton-accepting dimethylamino groups exhibited multicolor fluorescence ranging from near-infrared to blue by multistep protonations of the two substituents and the HBq moiety. Thus, our systematic modulation of the electronic structures of the HBq skeleton revealed that the photoacidity and photobasicity in the HBq moiety in both the ground and excited states are crucial in the excited-state geometry and photophysical properties of a derivative. The excited-state geometry is one of the most important factors to characterize the light-emitting properties of a molecule, and therefore, the present study provides a key insight toward the design of fluorescent molecules.

Author contributions

Conceptualization: M. M. and A. I.; syntheses and characterization: M. M.; spectroscopic and photophysical measurements/analyses: M. M. and A. I.; single-crystal XRD analyses: A. I.; writing – original draft: M. M.; writing – review and editing: M. M. and A. I.

Conflicts of interest

There are no conflicts to declare.

Data availability

The data supporting this study have been included as part of the supplementary information (SI). Supplementary information: ^{1}H-NMR and DFT/TD-DFT calculations for the derivatives; crystallographic data for **1NMe$_2$**, **1OMe**, **1Me**, **1H**, **1F** and **1CF$_3$**; data comparisons for the fluorescence properties of the derivatives; fluorescence characteristics of the derivatives in the crystalline phases; solvent dependences of the fluorescence spectra of **1Me**, **1F**, **1Cl**, **1CN** and **1NO$_2$**; photophysical properties of deuterated **1Me** and **1NO$_2$**; and TFA-addition data of the derivatives. See DOI: https://doi.org/10.1039/d5ra09266c.

CCDC 2505357–2505362 (**1NMe$_2$**, **1OMe**, **1Me**, **1H**, **1F** and **1CF$_3$**) contain the supplementary crystallographic data for this paper.[49a–f]

Acknowledgements

The authors acknowledge Dr Kazuaki Aburaya (Rigaku Corporation) for his support to solve the crystal structure of **1NMe$_2$**. MM acknowledges JST-SPRING (JPMJSP2141) for the financial support.

References

1 H. Jia, X. Gao, Y. Shi, N. Sayyadi, Z. Zhang, Q. Zhao, Q. Meng and R. Zhang, *Spectrochim. Acta, Part A*, 2015, **149**, 674–681.
2 H. Uoyama, K. Goushi, K. Shizu, H. Nomura and C. Adachi, *Nature*, 2012, **492**, 234–238.
3 C. Mayr, T. D. Schmidt and W. Brütting, *Appl. Phys. Lett.*, 2014, **105**, 183304.
4 O. S. Tiwari, V. Rawat, S. Rencus-Lazar and E. Gazit, *Spectrochim. Acta, Part A*, 2025, **326**, 125277.
5 K. Rotkiewicz, K. H. Grellmann and Z. R. Grabowski, *Chem. Phys. Lett.*, 1973, **19**, 315–318.
6 A. Ito, S. Ishizaka and N. Kitamura, *Phys. Chem. Chem. Phys.*, 2010, **12**, 6641–6649.
7 C. Yuan, S. Saito, C. Camacho, S. Irle, I. Hisaki and S. Yamaguchi, *J. Am. Chem. Soc.*, 2013, **135**, 8842–8845.
8 C. Yuan, S. Saito, C. Camacho, T. Kowalczyk, S. Irle and S. Yamaguchi, *Chem.–Eur. J.*, 2014, **20**, 2193–2200.
9 R. Kimura, H. Kuramochi, P. Liu, T. Yamakado, A. Osuka, T. Tahara and S. Saito, *Angew. Chem., Int. Ed.*, 2020, **59**, 16430–16435.
10 A. Weller, *Naturwissenschaften*, 1955, **42**, 175–176.
11 A. Weller and Z. Elektrochem, *Ber. Bunsenges. Phys. Chem.*, 1956, **60**, 1144–1147.
12 G. F. Kirkbright, D. E. M. Spillane, K. Anthony, R. G. Brown, J. D. Hepworth, K. W. Hodgson and M. A. West, *Anal. Chem.*, 1984, **56**, 1644–1647.
13 A. Heller and D. L. Williams, *J. Phys. Chem.*, 1970, **74**, 4473–4480.
14 N. Suzuki, A. Fukazawa, K. Nagura, S. Saito, H. Kitoh-Nishioka, D. Yokogawa, S. Irle and S. Yamaguchi, *Angew. Chem., Int. Ed.*, 2014, **53**, 8231–8235.
15 N. Suzuki, K. Suda, D. Yokogawa, H. Kitoh-Nishioka, S. Irle, A. Ando, L. M. G. Abegão, K. Kamada, A. Fukazawa and S. Yamaguchi, *Chem. Sci.*, 2018, **9**, 2666–2673.
16 L. Zhao, X. He, Y. Huang, J. Li, Y. Li, S. Tao, Y. Sun, X. Wang, P. Ma and D. Song, *Sens. Actuators, B*, 2019, **296**, 126571.
17 H. Ren, F. Huo, X. Wu, X. Liu and C. Yin, *Chem. Commun.*, 2021, **57**, 655–658.
18 Y. Ye, Q. Liu, K. She, M. Li, F. Luo and Y. Zhang, *Sens. Actuators, B*, 2025, **444**, 138471.
19 C. Y. Peng, J. Y. Shen, Y. T. Chen, P. J. Wu, W. Y. Hung, W. P. Hu and P.-T. Chou, *J. Am. Chem. Soc.*, 2015, **137**, 14349–14357.
20 S.-Z. Yi, B.-N. Li, P.-Y. Fu, M. Pan and C.-Y. Su, *ACS Appl. Mater. Interfaces*, 2023, **15**, 3172–3181.
21 K. Das, N. Sarkar, A. K. Ghosh, D. Majumdar, D. N. Nath and K. Bhattacharyya, *J. Phys. Chem. A*, 1994, **98**, 9126–9132.
22 O. K. Abou-Zied, R. Jimenez, E. H. Z. Thompson, D. P. Millar and F. E. Romesberg, *J. Phys. Chem. A*, 2002, **106**, 3665–3672.
23 M. Ikegami and T. Arai, *J. Chem. Soc., Perkin Trans. 2*, 2002, 1296–1301.
24 M. T. Ignasiak, C. Houee-Levin, G. Kciuk, B. Marciniak and T. Pedzinski, *ChemPhysChem*, 2015, **16**, 628–633.
25 G. Smulevich, P. Foggi, A. Feis and M. P. Marzocchi, *J. Chem. Phys.*, 1987, **87**, 5664–5669.
26 G. Smulevich and P. Foggi, *J. Chem. Phys.*, 1987, **87**, 5657–5663.
27 T. P. Smith, K. A. Zaklika, K. Thakur, G. C. Walker, K. Tominaga and P. F. Barbara, *J. Phys. Chem.*, 1991, **95**, 10465–10475.
28 S.-i. Nagaoka and U. Nagashima, *Chem. Phys.*, 1996, **206**, 353–362.
29 D. McMorrow and M. Kasha, *J. Phys. Chem.*, 1984, **88**, 2235–2243.
30 M. L. Martinez, W. C. Cooper and P.-T. Chou, *Chem. Phys. Lett.*, 1992, **193**, 151–154.
31 L. P. Hammett, *J. Am. Chem. Soc.*, 1937, **59**, 96–103.
32 O. V. Dolomanov, L. J. Bourhis, R. J. Gildea, J. A. K. Howard and H. Puschmann, *J. Appl. Crystallogr.*, 2009, **42**, 339–341.
33 G. M. Sheldrick, *Acta Crystallogr., Sect. A:Found. Adv.*, 2015, **A71**, 3–8.
34 G. M. Sheldrick, *Acta Crystallogr., Sect. C:Struct. Chem.*, 2015, **C71**, 3–8.
35 F. Duan, X. Li, S. Cai, G. Xin, Y. Wang, D. Du, S. He, B. Huang, X. Guo, H. Zhao, R. Zhang, L. Ma, Y. Liu, Q. Du, Z. Wei, Z. Xing, Y. Liang, X. Wu, C. Fan, C. Ji, D. Zeng, Q. Chen, Y. He, X. Liu and W. Huang, *J. Med. Chem.*, 2014, **57**, 3707–3714.
36 B. N. Briggs, F. Durola, D. R. McMillin and J.-P. Sauvage, *Can. J. Chem.*, 2011, **89**, 98–103.
37 J. Lee, C. H. Kim and T. Joo, *J. Phys. Chem. A*, 2013, **117**, 1400–1405.
38 m.p. 100.4–100.8 °C; ^{1}H-NMR ($CDCl_3$): δ = 14.9 (s, 1H, OH), 8.84 (dd, 1H, J = 1.7, 4.7 Hz, 2-Ar–H), 8.27 (dd, 1H, J = 1.7, 8.0 Hz, 4-Ar–H), 7.82 (d, 1H, J = 8.9 Hz, 5- or 6-Ar–H), 7.64 (d, 1H, J = 8.9 Hz, 5- or 6-Ar–H), 7.63 (t, 1H, J = 7.9 Hz, 8-Ar–H), 7.58 (dd, 1H, J = 4.7, 8.0 Hz, 3-Ar–H), 7.42 (dd, 1H, J = 1.0, 7.8 Hz, 9-Ar–H). 7.27–7.23 ppm (m, 1H, 7-Ar–H);

HRMS (ESI, positive mode): calcd for $[(M + H)]^+$: m/z = 196.0757; found: 196.0735; IR (KBr): $\tilde{\nu}$ = 3054 (Ar), 3026 (Ar), 2688 (OH), 1623 (Ar), 1584 (Ar), 1530 (Ar), 1470 (Ar), 1438 (Ar), 1420 (Ar), 1412 (Ar), 1392 (Ar), 1335 (Ar), 1273 (Ar), 1128 (Ar), 830 (Ar), 761 (Ar), 721 (Ar), 569 cm^{-1} (Ar).

39 M. J. Frisch, G. W. Trucks, H. B. Schlegel, G. E. Scuseria, M. A. Robb, J. R. Cheeseman, G. Scalmani, V. Barone, G. A. Petersson, H. Nakatsuji, X. Li, M. Caricato, A. V. Marenich, J. Bloino, B. G. Janesko, R. Gomperts, B. Mennucci, H. P. Hratchian, J. V. Ortiz, A. F. Izmaylov, J. L. Sonnenberg, D. Williams-Young, F. Ding, F. Lipparini, F. Egidi, J. Goings, B. Peng, A. Petrone, T. Henderson, D. Ranasinghe, V. G. Zakrzewski, J. Gao, N. Rega, G. Zheng, W. Liang, M. Hada, M. Ehara, K. Toyota, R. Fukuda, J. Hasegawa, M. Ishida, T. Nakajima, Y. Honda, O. Kitao, H. Nakai, T. Vreven, K. Throssell, J. A. Montgomery Jr, J. E. Peralta, F. Ogliaro, M. J. Bearpark, J. J. Heyd, E. N. Brothers, K. N. Kudin, V. N. Staroverov, T. A. Keith, R. Kobayashi, J. Normand, K. Raghavachari, A. P. Rendell, J. C. Burant, S. S. Iyengar, J. Tomasi, M. Cossi, J. M. Millam, M. Klene, C. Adamo, R. Cammi, J. W. Ochterski, R. L. Martin, K. Morokuma, O. Farkas, J. B. Foresman and D. J. Fox, *Gaussian 16, Revision A.03*, Gaussian, Inc., Wallingford, CT, 2016.

40 A. D. Becke, *J. Chem. Phys.*, 1993, **98**, 5648–5652.

41 P. J. Hay and W. R. Wadt, *J. Chem. Phys.*, 1985, **82**, 299–310.

42 V. Barone and M. Co, *J. Phys. Chem. A*, 1998, **102**, 1995–2001.

43 R. Dennington, T. A. Keith and J. M. Millam, *GaussView, Version 6.0.16*, Semichem Inc., Shawnee Mission, KS, 2016.

44 B. M. E. Rozycka-Sokolowska and V. Pavlyuk, *Acta Crystallogr.*, 2004, **60**, o884–o885.

45 R. Englman and J. Jortner, *Mol. Phys.*, 1970, **18**, 145–164.

46 S.-H. Son, Y. Abe, M. Yuasa, Y. Yamagishi, N. Sakai, T. Ayabe and K. Yamada, *Chem. Lett.*, 2011, **40**, 378–380.

47 H. A. Z. Sabek, A. M. M. Alazaly, D. Salah, H. S. Abdel-Samad, M. A. Ismail and A. A. Abdel-Shafi, *RSC Adv.*, 2020, **10**, 43459–43471.

48 M. Miwa and A. Ito, *RSC Adv.*, 2025, **15**, 46297–46307.

49 (*a*) CCDC 2505357: Experimental Crystal Structure Determination, 2026, DOI: 10.5517/ccdc.csd.cc2q30zv; (*b*) CCDC 2505358: Experimental Crystal Structure Determination, 2026, DOI: 10.5517/ccdc.csd.cc2q310x; (*c*) CCDC 2505359: Experimental Crystal Structure Determination, 2026, DOI: 10.5517/ccdc.csd.cc2q311y; (*d*) CCDC 2505360: Experimental Crystal Structure Determination, 2026, DOI: 10.5517/ccdc.csd.cc2q312z; (*e*) CCDC 2505361: Experimental Crystal Structure Determination, 2026, DOI: 10.5517/ccdc.csd.cc2q3130; (*f*) CCDC 2505362: Experimental Crystal Structure Determination, 2026, DOI: 10.5517/ccdc.csd.cc2q3141.